Applied Catalysis B: Environmental 291 (2021) 120125

Contents lists available at ScienceDirect

Applied Catalysis B: Environmental

journal homepage: www.elsevier.com/locate/apcatb

Introducing tin to develop ternary metal oxides with excellent hydrothermal stability for NH_3 selective catalytic reduction of NO_x

Jingjing Liu [a], Guangzhi He [a,d], Wenpo Shan [b,*], Yunbo Yu [a,b,d], Yanlong Huo [a,d], Yan Zhang [b], Meng Wang [b,d], Rong Yu [c], Shengsheng Liu [c], Hong He [a,b,d,**]

[a] State Key Joint Laboratory of Environment Simulation and Pollution Control, Research Center for Eco-Environmental Sciences, Chinese Academy of Sciences, Beijing, 100085, China

[b] Center for Excellence in Regional Atmospheric Environment, Institute of Urban Environment, Chinese Academy of Sciences, Xiamen, 361021, China

[c] National Center for Electron Microscopy in Beijing, School of Materials Science and Engineering, Key Laboratory of Advanced Materials of Ministry of Education of China, State Key Laboratory of New Ceramics and Fine Processing, Tsinghua University, Beijing, 100084, China

[d] University of Chinese Academy of Sciences, Beijing, 100049, China

ARTICLE INFO

Keywords:
Heterogeneous catalysis
NO_x removal
Hydrothermal stability
Anti-sintering
SnO_2

ABSTRACT

Thermal stability is crucial for the practical application of heterogeneous catalysts. In particular, the development of catalysts with excellent hydrothermal stability remains a big challenge for diesel exhaust after-treatment technologies. Here, we synthesized a $Ce_1W_{0.24}Sn_2O_x$ catalyst with high hydrothermal stability for the NO_x removal from diesel engines. The catalyst shows >90 % NO_x conversion at 300−550 °C even after an extreme aging treatment at 1000 °C, with much better hydrothermal stability than the $Ce_1W_{0.24}O_x$ catalyst and the commercial catalysts such as Cu-SSZ-13 and V_2O_5-WO_3/TiO_2. The experimental and theoretical results reveal that the SnO_2-related particles modified by W and Ce species show outstanding sintering resistance at high temperature, which provides sufficient Ce-W active phase for the catalytic reaction. This study may provide new opportunities for the application of metal oxide catalysts for diesel engine NO_x emission control and a new idea for the development of catalysts with high thermal stability.

1. Introduction

Currently, catalysis plays a crucial role in chemical industry, energy production, and removal of environmental pollutants [1,2]. To this aim, the development of catalysts with desired structures/functions is at the center of catalysis. Catalysts in the aforementioned applications often work under harsh conditions at extremely high temperature. As a result, developing catalysts with high thermal stability that can maintain activity and selectivity over long-term catalytic operation is one of the main challenges for practical applications [3,4]. This challenge is especially pronounced in the fabrication of promising after-treatment catalysts for the control of emissions from internal combustion engines in environmental catalysis [5]. For gasoline engine after-treatment, three-way catalysts (TWCs) have been successfully applied, which should be active even after thermal aging at 1000 °C [6]. Compared with gasoline engines, diesel engines have helped to decrease the reliance on fossil fuels and combatted the dangers of global climate change due to their superior fuel efficiency and greenhouse gas reduction potential [7]. For diesel engines, however, lean burn operation results in high emission of nitrogen oxides (NO_x), which makes a great contribution to the formation of acid rain, haze, and ozone, as well as human diseases [8]. Selective catalytic reduction of NO_x with ammonia (NH_3-SCR) is the dominant technology for NO_x emission control from diesel engines [5]. To meet the current EU VI diesel emission standards, furthermore, the NH_3-SCR reactor is usually installed downstream of the diesel particulate filter (DPF). When the DPF is regenerated to remove the collected particulate matter, the peak temperature at the end of the DPF can even reach 1000 °C [9]. Thus, stabilizing the active component of NH_3-SCR

* Corresponding author at: Center for Excellence in Regional Atmospheric Environment, Institute of Urban Environment, Chinese Academy of Sciences, Xiamen, 361021, China.

** Corresponding author at: State Key Joint Laboratory of Environment Simulation and Pollution Control, Research Center for Eco-Environmental Sciences, Chinese Academy of Sciences, Beijing, 100085, China; Center for Excellence in Regional Atmospheric Environment, Institute of Urban Environment, Chinese Academy of Sciences, Xiamen, 361021, China.

E-mail addresses: wpshan@iue.ac.cn (W. Shan), honghe@rcees.ac.cn (H. He).

https://doi.org/10.1016/j.apcatb.2021.120125
Received 4 December 2020; Received in revised form 15 February 2021; Accepted 5 March 2021
Available online 9 March 2021

catalyst under thermal shock is a challenging task. In this case, despite its high cost, copper ion-exchanged SSZ-13 zeolite (Cu-SSZ-13) is the most prominent catalyst owing to its superior DeNO$_x$ efficiency and thermal durability [10,11]. After being hydrothermally aged at temperatures higher than 850 °C, however, the NO$_x$ conversion of the Cu-SSZ-13 catalyst as well as other ion-exchanged zeolites still suffers from a cliff-like drop stemming from the dealumination process and the formation of inactive Cu-Al clusters and CuO$_x$ [12–15]. To meet the requirements of practical applications on diesel vehicles, therefore, it is urgent to develop NH$_3$-SCR catalysts with higher hydrothermal stability.

Generally, metal oxides such as the V- and Ce- based catalysts are highly active for the NH$_3$-SCR process [16–19]. After harsh thermal- or hydrothermal- aging treatment, however, the metal oxides often suffer from severe thermal sintering (particle migration and coalescence or Ostwald ripening) and/or chemical transformation of catalytic phases to non-catalytic phases, resulting in a severe decrease or even total loss of active catalytic sites. Due to thermal stability concerns, metal oxides were identified as unsuitable for NO$_x$ removal from diesel engines with an upstream DPF [20]. However, researchers have never stopped trying to develop sinter-resistant metal oxide NH$_3$-SCR catalysts. To inhibit the thermal degradation process of metal oxide catalysts, the screening and addition of thermally stable promoters to decrease the sintering rates of the catalysts was the principal approach.

As with all catalysts based on metal oxides, principally, both the redox sites and acid sites are necessary and should work together during the NH$_3$-SCR process [21,22]. Therefore, plenty of these dual functional sites with close coupling are essential for the development of NH$_3$-SCR catalysts with high catalytic activity. With this principle in mind, it can be predicted that the stability of the closely coupled structure will be crucial for developing metal oxide catalysts that are highly stable against thermal aging. Recently, it was found that CeW-based oxide catalysts with closely coupled cerium (as redox component) and tungsten (as acid component) exhibited excellent NH$_3$-SCR activity, but the hydrothermal stability still needs to be improved [23–25]. SnO$_2$-based materials displayed superior anti-sintering properties after being doped by a small amount of additive. For example, SnO$_2$ crystals being doped by Si, Mo, W, Nb or P were able to keep the crystal size below 10 nm during sintering up to 900 °C [26]. The high thermal stability of SnO$_2$-based materials is very attractive for the development of NH$_3$-SCR catalysts for NO$_x$ removal from diesel exhaust. Besides, SnO$_2$ possesses a high density of surface defects and relatively strong acidity, which were closely correlated with the formation of catalytically active oxygen species and the adsorption-activation of NH$_3$ on the surface [27,28]. The enhancing effects of Sn modification on the low-temperature catalytic activity and sulfur resistance of Ce-based catalysts have been confirmed in the past decade [29,30]. Recently, Li et al. reported that Sn shows stabilizing effects on the V-based catalyst [31]. The effects of Sn introduction on the hydrothermal stability of Ce-based catalysts, however, still needs to be further elucidated. As a result, a Ce-W-Sn ternary oxide catalyst with exceptional hydrothermal stability was successfully prepared and the stabilization mechanism was investigated by different methods. On the obtained catalyst, the Ce-W dual functional sites are stable even after an extreme hydrothermal aging treatment at 1000 °C, resulting in high hydrothermal stability.

2. Experimental section

2.1. Catalyst synthesis

The $Ce_1W_{0.24}Sn_\gamma O_x$ mixed oxides with different Sn doping amounts (γ = 1.0, 1.5, 2.0, 2.5 and 3.0) was obtained by a co-precipitation method. Exact quantities of ammonium metatungstate, cerium nitrate and tin tetrachloride were dissolved in 200 mL deionized water to obtain a transparent solution with total metallic ion concentration of 0.3 mol/L, and then excess ammonium hydroxide was added, resulting in the precipitation of a solid. After being stirred intensely at room temperature for 12 h, the precipitated solids were collected by filtration and then washed with distilled water until no Cl^- was detected by reaction with $AgNO_3$ solution (1 mol L^{-1}), followed by drying at 100 °C for 12 h. As shown by the TG-DSC curve of the $Ce_1W_{0.24}Sn_2O_x$ precursor (Fig. S1), the weight loss happened over a wide region of 50−700 °C. However, only one exothermal peak centered at 720 °C was detected above 700 °C, and no weight change was observed in the corresponding region. Therefore, the obtained precursor in this study was calcined in air at 800 °C for 3 h to transform into an active catalyst for the NH$_3$-SCR reaction.

For comparison, reference samples of $Ce_1W_{0.24}O_x$, $Ce_1Sn_2O_x$, pure CeO$_2$ and pure SnO$_2$ were prepared by the same method. The $W_{0.24}Sn_2O_x$ and pure WO$_3$ reference samples were prepared by direct evaporation of a W-Sn aqueous solution and W aqueous solution, respectively, followed by calcination at 800 °C for 3 h, as it is hard to realize the precipitation of W-Sn or W when using ammonium metatungstate as precursor.

2.2. Hydrothermal aging treatment

To predict the long-term hydrothermal stability, accelerated hydrothermal-aging treatment of the fresh $Ce_1W_{0.24}O_x$ and $Ce_1W_{0.24}Sn_2O_x$ catalysts was performed at 800−1000 °C for 3−16 h in a home-made aging device that consisted of a tube furnace, mass flow controllers, and a temperature and gas flow regulating system. The feed gas for hydrothermal aging (HA) treatment was composed of 10 vol. % H$_2$O balanced by air of 1 L min^{-1}. Typically, 1 g catalyst was hydrothermally aged at 800/900 °C for 16 h or 1000 °C for 3 h, respectively, denoted as $Ce_1W_{0.24}O_x$-800/900/1000HA and $Ce_1W_{0.24}Sn_2O_x$-800/900/1000HA. Cu-SSZ-13 (with SiO_2/Al_2O_3 molar ratio of 8.3 and Cu loading amount of 3.8 wt.%) by one-pot synthesis coupling with an ion exchange method [32] and 1 wt.% V_2O_5 - 8 wt.% WO_3/TiO_2 by incipient wetness impregnation method were also hydrothermally aged under the same conditions and denoted as Cu-SSZ-13-800/900/1000HA and V_2O_5-WO_3/TiO_2-800/900/1000HA, respectively.

2.3. NH$_3$-SCR performance tests

The steady state NH$_3$-SCR activity of catalysts was tested in a fixed-bed quartz tube reactor in the temperature range of 150−550 °C. Before activity tests, the catalysts were crushed and sieved to 40–60 mesh. In NH$_3$-SCR reactions, the model flow gas consisted of 500 ppm NO, 530 ppm NH$_3$, 5 vol. % O$_2$, and 5 vol. % H$_2$O balanced with N$_2$. The gas flow rate was kept at 500 mL/min and the catalyst mass was 500 mg, which corresponded to a gas hourly space velocity (GHSV) of 120, 000 h^{-1}. The concentrations of NO, NH$_3$, NO$_2$, and N$_2$O were continually monitored by an FTIR spectrometer (IS10 Nicolet), which was equipped with a multiple path gas cell (2 m). The NO$_x$ conversion and N$_2$ selectivity were calculated as follows:

$$NO_x\ conversion = \left(1 - \frac{[NO_x]_{out}}{[NO_x]_{in}}\right) \times 100\% \quad (1)$$

$$N_2\ selectively = \left(1 - \frac{2[N_2O]_{out}}{\left([NO_x]_{in} - [NO_x]_{out}\right) + \left([NH_3]_{in} - [NH_3]_{out}\right)}\right) \times 100\% \quad (2)$$

where, $[NO_x]_= [NO]+[NO_2]$, $[NO_x]_{in}$ and $[NO_x]_{out}$ denote the inlet and outlet gas concentrations of NO$_x$, respectively.

2.4. Kinetic analysis

The kinetic experiments for SCR reaction were evaluated in the same fixed-bed reactor as the activity test. The NO$_x$ conversion was kept at less than 20 % in the temperature range of 195−245 °C. The reaction rates of NO$_x$ conversion normalized by the surface area ($-R_{NOx}$, in mol s^{-1} m^{-2})

were calculated as follows:

$$-R_{NO_x} = \frac{F_{NO_x} \times x}{W \times A} \quad (3)$$

where, F_{NOx} is the molar flow rate of NO_x (in mol s^{-1}), x is the conversion of NO_x, W is the weight of catalyst (in g), and A is the surface area of catalyst (in m^2 g^{-1}). The apparent activation energies (E_a, in kJ mol^{-1}) can be calculated from the Arrhenius plots of the reaction rates.

2.5. Catalyst characterization and theoretical calculations

Phase structures of the catalysts were investigated by X-ray diffraction (XRD) patterns collected with a Bruker D8 Advance diffractometer equipped with a Cu Kα X-ray tube operated at 40 kV and 40 mA using a step size of 0.02° and a time per step of 0.6 s. Experimental fitting of the XRD patterns was carried out from 10−90° 2θ using TOPAS V5.0. The lattice parameters and mean crystallite size were obtained from Rietveld refinement assuming a tetragonal SnO_2 cell and a cubic CeO_2 cell for $Ce_1W_{0.24}Sn_2O_x$ catalysts. X−ray photoelectron spectroscopy (XPS) measurements were carried out on an X−ray photoelectron spectrometer (AXIS Supra/Ultra) with Al Kα radiation (1486.7 eV). The binding energies were referenced to the C 1s line at 284.8 eV. Quantification of the Ce, W, Sn and O atomic fractions on the surface was obtained from the integration of Ce 3d, W 4f, Sn 3d and O 1s core level spectra with appropriate corrections for sensitivity factors. The elemental compositions were analyzed *via* X-ray fluorescence analysis (XRF) on a Thermo Fisher ARL Perform' X 4200 with maximum voltage of 70 KV. High-angle annular dark field-scanning transmission electron microscope (HAADF-STEM) investigation was performed on a Titan Cubed Themis G2 300 Double Aberration-Corrected transmission electron microscope, which was equipped with X-Field Emission Gun with Monochromator. The W L_3-edge X-ray absorption fine structure (XAFS) spectra of standards and $Ce_1W_{0.24}Sn_2O_x$ catalysts were collected at the beamline BL1W1B of the Beijing Synchrotron Radiation Facility (BSRF). The typical energy of the storage ring was 1.5 GeV, and the electron current was 180 mA in the top-up mode. The white light was monochromatized by a Si (111) double-crystal monochromator and calibrated with a W foil (L_3 edge 10207 eV). Samples were pressed into thin slices, and positioned at 90° to the incident beam in the sample-holder. The XAFS spectra were recorded in transmission mode with two ion chambers. XAFS data were processed using the Athena and Artemis modules. The spectra were normalized using Athena firstly, and then shell fittings were performed with Artemis. The χ(k) function was Fourier transformed (FT) using k^3 weighting, and all fittings were done in R-space. The amplitude reduction factor (S_0^2) was estimated to be 0.827 according to the fitting results of the W foil. The coordination parameters of sorption samples were obtained by fitting the experimental peaks with theoretical amplitude. *In situ* Raman spectroscopy was used to obtain the short-range structure of the catalysts on a homemade UV resonance Raman spectrometer (UVR DLPC-DL-03), which was calibrated against the Stokes Raman signal of Teflon at 1378 cm^{-1}. A 532 nm He-Cd laser beam was used as the excitation source for the measurement of Raman intensity. After dehydration at 300 °C for 1 h in flowing O_2 (100 mL/min), the Raman spectra were collected at 300 °C. Scan numbers of 40 and scan speed 40 s/scan were selected for spectrum collection.

Density functional theory (DFT) calculations with periodic boundary conditions (PBC) were performed using the Perdew-Burke-Ernzerhof (PBE) functional [33] as implemented in the Vienna *ab initio* simulation package (VASP 5.4.4) [34]. The projector augmented wave method (PAW) was used to describe the core-valence electron interaction. All calculations were spin-polarized. The details about DFT calculations as well as other characterization methods, including N_2 adsorption-desorption analysis, *in situ* high temperature XRD (*in situ* HTXRD) experiments, H_2 temperature program reduction (H_2-TPR) experiments, NH_3 temperature program desorption (NH_3-TPD) experiments, high-resolution transmission electron microscope (HR-TEM) and thermal gravimetric and differential scanning calorimetry (TG-DSC) analysis, can be found in the Supplemental Material.

3. Results

3.1. NH_3-SCR performance and hydrothermal stability

Compared with other $Ce_1W_{0.24}Sn_yO_x$ catalysts, the $Ce_1W_{0.24}Sn_2O_x$ catalyst with the Ce: W: Sn molar ratio of 1: 0.24: 2 showed the highest NO_x conversion and was selected for the tests of hydrothermal-aging stability in this study (Fig. S2). The fresh $Ce_1W_{0.24}Sn_2O_x$ catalyst possessed NH_3-SCR performance superior to those of the corresponding pure oxides and binary ones at 150−450 °C (Fig. 1a). An activity drop was observed when the reaction temperature exceeded 450 °C due to the occurrence of NH_3 oxidation [35]. After being further hydrothermally aged under different harsh conditions (800/900 °C for 16 h or 1000 °C for 3 h), the $Ce_1W_{0.24}Sn_2O_x$ catalysts still removed >90 % NO_x from simulated diesel exhaust at 300−500 °C (Fig. 1b), accompanying with low concentrations of N_2O by-products (Fig. S3). After being hydrothermally aged under the same conditions, the state-of-the-art NH_3-SCR catalysts including commercial Cu-SSZ-13 and V_2O_5-WO_3/TiO_2 catalysts, however, had already lost their $DeNO_x$ activities substantially (Figs. 1b and S4). A severe deactivation process also occurred for the pristine $Ce_1W_{0.24}O_x$ catalysts with the increase of aging temperature (Fig. 1c), which in turn demonstrated the crucial role of the Sn component in improving the hydrothermal stability. The NO_x conversions of $Ce_1W_{0.24}O_x$ and $Ce_1W_{0.24}Sn_2O_x$ catalysts in the low-temperature range were much higher than those of $Ce_1Sn_2O_x$ and $W_{0.24}Sn_2O_x$ catalysts (Fig. 1a), suggesting that Ce-W served as the main active phase instead of Ce-Sn and W-Sn species below 300 °C for the $Ce_1W_{0.24}Sn_2O_x$ catalyst. According to the kinetic analysis results, the $Ce_1W_{0.24}O_x$ and $Ce_1W_{0.24}Sn_2O_x$ catalysts showed similar apparent activation energies (E_a) in the range 195−245 °C (Fig. 1d). It might be deduced that the introduction of Sn to $Ce_1W_{0.24}O_x$ had little effect on the active catalytic sites for the NH_3-SCR reaction. Additionally, hydrothermal aging treatment had induced little effect on the E_a and the NH_3-SCR reaction rate per unit area of $Ce_1W_{0.24}O_x$ and $Ce_1W_{0.24}Sn_2O_x$ catalysts, indicating the stability of Ce-W active sites. Therefore, the excellent hydrothermal stability of the $Ce_1W_{0.24}Sn_2O_x$ catalyst should mainly origin from its sintering resistance.

3.2. Structural property

The $Ce_1W_{0.24}Sn_2O_x$ catalyst showed much higher surface area and pore volume than the $Ce_1W_{0.24}O_x$ catalyst (Fig. 2), as calculated from the corresponding N_2 adsorption-desorption isotherms (Fig. S5). Although the hydrothermal aging treatment induced a decrease in the BET surface area (S_{BET}) and total pore volume (V_{total}), the sintering process of the $Ce_1W_{0.24}Sn_2O_x$ catalyst was remarkably suppressed compared with the $Ce_1W_{0.24}O_x$ catalyst, indicating that the thermal stability of the $Ce_1W_{0.24}O_x$ catalyst was improved by the introduction of Sn species, which is beneficial to the improvement of NO_x removal efficiency. X-ray diffraction (XRD) analysis was carried out to investigate the phase composition of the catalysts, and the mean crystallite size of each phase was calculated by Rietveld refinement. For the $Ce_1W_{0.24}O_x$ catalyst, both cubic CeO_2 (*c*-CeO_2) and orthorhombic $Ce_4W_9O_{33}$ [36] phases were detected (Fig. 3a). After hydrothermal treatment at 800 °C for 16 h, this catalyst underwent significant sintering as indicated by the sharper XRD pattern of $Ce_1W_{0.24}O_x$-800HA than that of the original $Ce_1W_{0.24}O_x$ catalyst. When the aging temperature further increased to 900 and 1000 °C, besides this severe sintering phenomenon, a phase transition from $Ce_4W_9O_{33}$ to $Ce_2(WO_4)_3$ was also observed for $Ce_1W_{0.24}O_x$ catalyst. With the introduction of Sn into the $Ce_1W_{0.24}O_x$ catalyst, only broad XRD patterns indexed to the *c*-CeO_2 and tetragonal SnO_2 (*t*-SnO_2) phases were detected for the $Ce_1W_{0.24}Sn_2O_x$ catalyst (Fig. 3b). As no diffraction

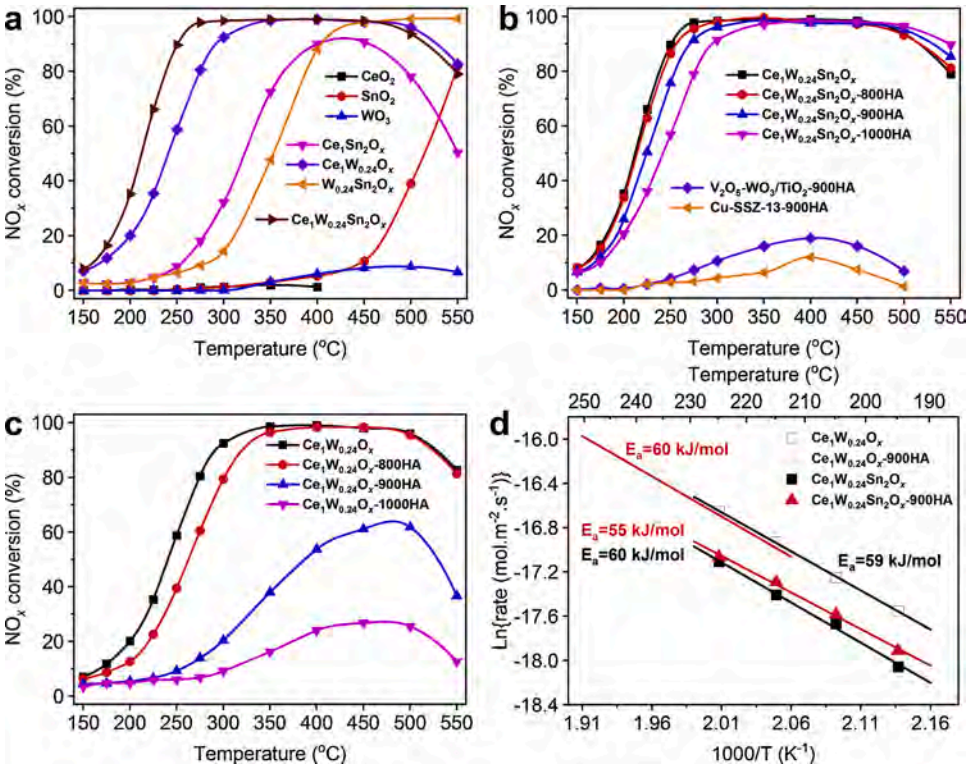

Fig. 1. NH_3-SCR behaviors of fresh and hydrothermally aged catalysts as a function of temperature. (a) The NO_x conversion of fresh catalysts with different elemental composition. (b) The NO_x conversion of hydrothermally aged $Ce_1W_{0.24}Sn_2O_x$, V_2O_5-WO_3/TiO_2 and Cu-SSZ-13 catalysts. (c) The NO_x conversion of hydrothermally aged $Ce_1W_{0.24}O_x$ catalysts. (d) The Arrhenius plots of fresh and hydrothermally aged $Ce_1W_{0.24}O_x$ and $Ce_1W_{0.24}Sn_2O_x$ catalysts. The reported values are measured under steady state. Test conditions of the steady state NH_3-SCR activities: 500 ppm NO, 530 ppm NH_3, 5 vol. % O_2, 5 vol. % H_2O, balanced N_2, and GHSV = 120,000 h^{-1}.

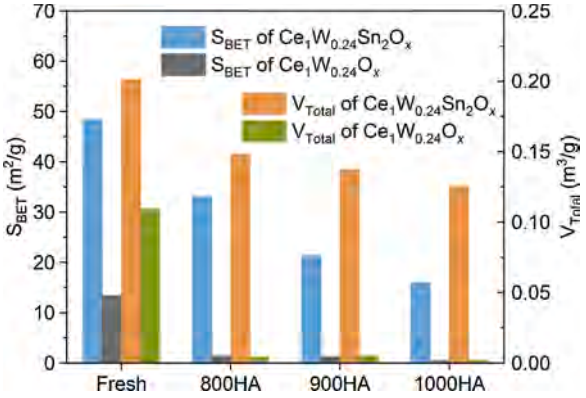

Fig. 2. The specific surface area (S_{BET}, left axis) and total pore volume (V_{total}, right axis) determined from nitrogen adsorption-desorption analysis for fresh and hydrothermally aged $Ce_1W_{0.24}O_x$ and $Ce_1W_{0.24}Sn_2O_x$ catalysts.

peaks corresponding to W-related crystalline phases were observed, the tungsten species in the $Ce_1W_{0.24}Sn_2O_x$ catalyst must exist in a highly dispersed state. Additionally, hydrothermal aging treatments at 800/900 °C for 16 h or 1000 °C for 3 h hardly changed the phase composition of $Ce_1W_{0.24}Sn_2O_x$ catalysts. Rietveld refinement for $Ce_1W_{0.24}Sn_2O_x$ catalysts also confirmed the two-phase structure consisting *c*-CeO_2 and *t*-SnO_2 phases (Fig. 4a and S6). With the increase of the hydrothermal aging temperature, rapid grain growth occurred for the *c*-CeO_2 phase, while the grain size of the *t*-SnO_2 phase still remained at nanoscale (< 22 nm) even after being hydrothermally aged at 1000 °C for 3 h (Fig. 4b). Such significant difference in crystallization indicated that the *t*-SnO_2 phase in the $Ce_1W_{0.24}Sn_2O_x$ catalyst played a crucial role in its sintering resistance.

To further investigate the structure of the crystalline phases in $Ce_1W_{0.24}Sn_2O_x$ catalysts, the lattice parameters of *c*-CeO_2 and *t*-SnO_2 phases were extracted from the corresponding Rietveld refinement results. The lattice constants of *c*-CeO_2 for $Ce_1W_{0.24}Sn_2O_x$ catalysts were in good accordance with that of pure CeO_2 (Table S1), which indicated that no modification to the bulk *c*-CeO_2 phase occurred for these catalysts.

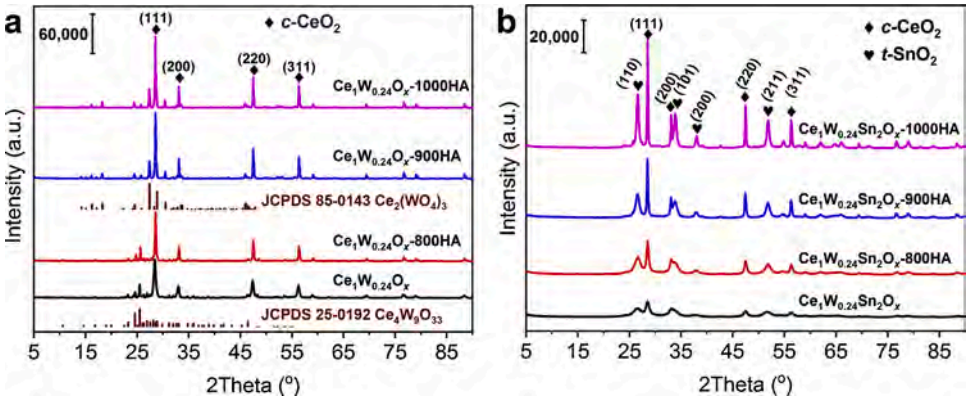

Fig. 3. The XRD patterns of fresh and hydrothermally aged (a) $Ce_1W_{0.24}O_x$ and (b) $Ce_1W_{0.24}Sn_2O_x$ catalysts.

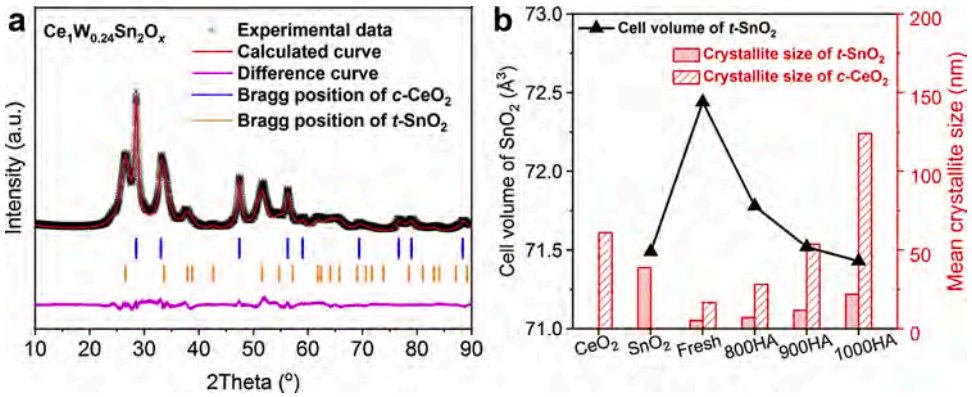

Fig. 4. Rietveld refinement analysis. (a) The Rietveld refinement profiles for $Ce_1W_{0.24}Sn_2O_x$ catalyst. (b) The cell volume of *t*-SnO_2 phase (left axis, line chart) and mean crystallite size of *c*-CeO_2 and *t*-SnO_2 phases (right axis, column chart) for $Ce_1W_{0.24}Sn_2O_x$ catalysts determined from Rietveld refinement of corresponding XRD patterns.

The cell volumes (V_{SnO2}) of *t*-SnO_2, however, were larger than for the pure SnO_2 sample (Table S1), indicating the occurrence of lattice expansion. As the Shannon ionic radii of six-coordinated Ce^{4+}, Sn^{4+} and W^{6+} are 0.87, 0.69 and 0.6 Å, respectively [37], the expansion of the *t*-SnO_2 cell should be caused by the incorporation of Ce^{4+} into the SnO_2 lattice, which resulted in the formation of a Ce-Sn solid solution [38]. The value of V_{SnO2} decreased with increasing hydrothermal aging temperature (Fig. 4b), which suggested that a relaxation phenomenon occurred under the hot, humid atmosphere, driving the Ce from the *t*-SnO_2 inner lattice sites towards its surface [39]. This part of the Ce species can be in close contact with W species on the SnO_2 surface, and provides high-efficiency active sites for the NH_3-SCR reaction. A previous study revealed that Ce-doped SnO_2 possessed high thermal stability below 900 °C [39]. In our case, the formation of a metastable Ce-Sn solid solution as mentioned above was also beneficial for the inhibition of SnO_2 particle grain growth in the $Ce_1W_{0.24}Sn_2O_x$ catalyst. *In situ* high temperature X-ray diffraction (*in situ* HTXRD) was used to further investigate the phase evolution and thermal stability. Crystalline phases related to Ce-W compounds [40] easily formed from the $Ce_1W_{0.24}O_x$ precursor when the temperature reached 750 °C (Figs. 5a and S7a). With this facile phase transformation in mind, it is reasonable that the catalytic activity of the $Ce_1W_{0.24}O_x$ catalyst significantly decreased after experiencing high temperature. Besides, the solid-solid reaction between CeO_2 and WO_x to form Ce-W crystal phases was accompanied by the release of oxygen (e.g. $4CeO_2+9WO_x \rightarrow Ce_4W_9O_{33}+0.5\times(9x-25)O_2$, $4CeO_2 + 2(Ce_4W_9O_{33}) \rightarrow 6(Ce_2(WO_4)_3)+O_2$), which would block the redox cycle between Ce^{3+} and Ce^{4+} by an oxygen release-storage process. For the $Ce_1W_{0.24}Sn_2O_x$ precursor, however, no crystalline phase related to any Ce-W compound was observed up to 900 °C (Figs. 5b and S7b). The XRD diffractograms of cubic $Ce_2W_2O_9$ (*c*-$Ce_2W_2O_9$) were observed at 950 and 1000 °C and then completely disappeared when the temperature cooled to room temperature (30 °C). The sintering and redispersion property of Ce-W species in the $Ce_1W_{0.24}Sn_2O_x$ catalyst ruled out the possibility of thermal sintering caused by *c*-$Ce_2W_2O_9$ phase. Meanwhile, the recoverability of Ce-W species in the $Ce_1W_{0.24}Sn_2O_x$ precursor against heat treatment under such a harsh

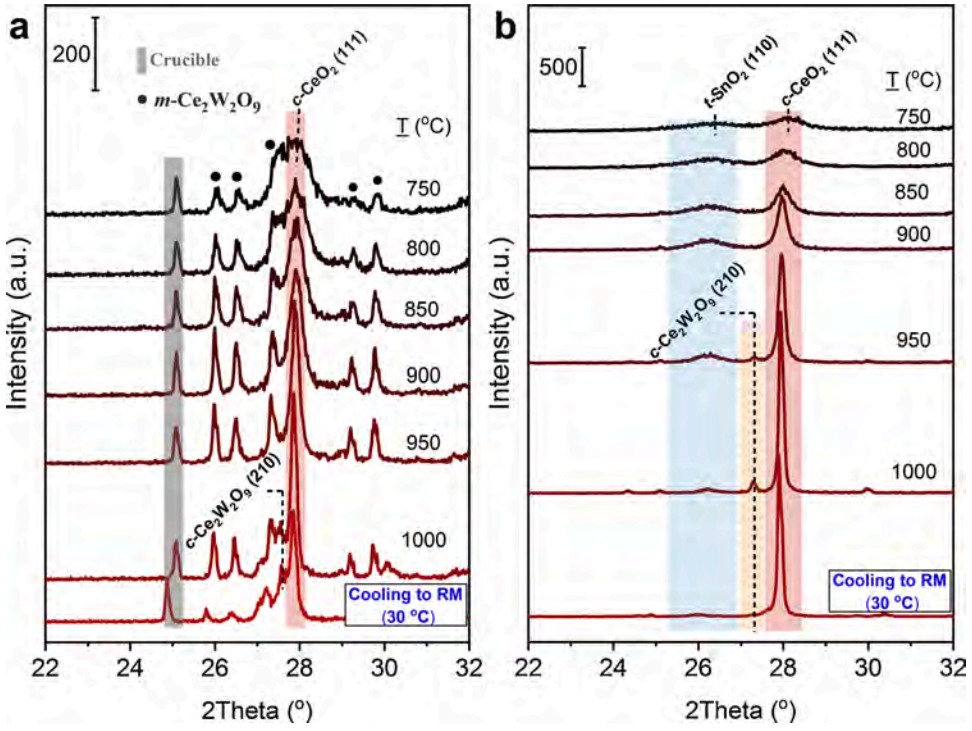

Fig. 5. The *in situ* high temperature X-ray diffraction patterns of (a) $Ce_1W_{0.24}O_x$ and (b) $Ce_1W_{0.24}Sn_2O_x$ precursors.

environment benefited the preservation of the redox properties of the $Ce_1W_{0.24}Sn_2O_x$ catalyst for the NH_3-SCR reaction.

3.3. Composition and distribution

The surface and bulk elemental compositions of catalysts in this work were measured respectively by X-ray photoelectron spectroscopy (XPS) and X-ray fluorescence (XRF) method (Fig. S8 and Table S2). The surface W/(Ce + W+Sn) molar ratio for the $Ce_1W_{0.24}Sn_2O_x$ catalyst was higher than the bulk one (Fig. 6a), suggesting that W species in $Ce_1W_{0.24}Sn_2O_x$ catalyst were mainly distributed on the surface. This surface enrichment of W species became more pronounced with increasing hydrothermal aging temperature (Fig. 6a). The elemental dispersion and configuration of the $Ce_1W_{0.24}Sn_2O_x$ catalyst were further revealed *via* high angle annular dark field-scanning transmission electron microscope (HAADF-STEM) images. As shown in Fig. 6b–e, the components of W and Ce kept in close contact and were evenly dispersed on the SnO_2-rich particles of the $Ce_1W_{0.24}Sn_2O_x$ catalyst. It can be inferred from the Rietveld refinement and abovementioned elemental distribution results that the W species on the surface of SnO_2 particles in the $Ce_1W_{0.24}Sn_2O_x$ catalyst would come in contact with the Ce species that were released from the *t*-SnO_2 lattice during hydrothermal aging treatment, thus playing an indispensable role in the retention of NH_3-SCR activity for the hydrothermally aged $Ce_1W_{0.24}Sn_2O_x$ catalyst. It has been suggested that the intensity contributed by an atom in HAADF images is roughly proportional to Z^2, where Z is the atomic number [41]. In the atomic resolution HAADF images, indeed, highly dispersed bright flecks highlighted by green circles were successfully detected on SnO_2 particles in $Ce_1W_{0.24}Sn_2O_x$ catalyst (Fig. 6f). Considering the higher Z values of Ce (58) and W(74) than Sn(50), these flecks were attributed to direct structural imaging information of $CeWO_x$-related species [42].

To further investigate the local structure around W atoms, Fourier transforms of the W L_3-edge extended X-ray absorption fine-structure (W L_3-edge FT-EXAFS) oscillations of $Ce_1W_{0.24}Sn_2O_x$ catalysts and standard samples (WO_3 and W foil) were fitted by the IFEFFIT software. Three candidate models were used for fitting the $Ce_1W_{0.24}Sn_2O_x$ catalyst, and the best-fit EXAFS data were obtained by model A as evidenced by its lowest R-factor (Table S3). To be specific, there was a W—O contribution at 1.76 Å with a coordination number close to 3.8 for the first shell, and a W-Ce contribution at 3.29 Å with a coordination number of 7.5 for the second shell. These fitting results suggested that the surface W species for the $Ce_1W_{0.24}Sn_2O_x$ catalyst were in a WO_4 tetrahedral coordination environment and mainly coupled with Ce by W-O-Ce structures on the surface, which agreed well with the HAADF-STEM results. The aforementioned W coordination mode in the $Ce_1W_{0.24}Sn_2O_x$ catalyst stayed almost unchanged after the hydrothermal aging treatment according to the EXAFS results of $Ce_1W_{0.24}Sn_2O_x$-800/900/1000HA catalysts (Fig. 7a and Table S3), and the stability of surface W species was further confirmed by *in situ* Raman spectra (Fig. 7b). The adsorption of NH_3 is an indispensable step for the NH_3-SCR reaction, which usually occurred on the acid sites origining from W═O species for CeW-based catalysts [24]. In this study, two high-frequency modes in the wavenumber range of 900−1100 cm^{-1} relating to the stretching vibration of terminal W═O species on the surface were observed for the fresh $Ce_1W_{0.24}Sn_2O_x$ catalyst (Fig. 7b). After being hydrothermally aged at 800/900 °C for 16 h, the Raman peaks related to W species for $Ce_1W_{0.24}Sn_2O_x$ catalysts showed little change.

3.4. Redox ability and acidity

The redox ability and acidity of catalysts were investigated by the H_2-TPR and NH_3-TPD methods, respectively. As shown in Fig. 8a, the two broad peaks with low intensity centered at 489 and 797 °C for the CeO_2 sample were due to the reduction of ceria at the surface and in the bulk phase, respectively [43]. After W addition, the reduction peak of surface ceria was centered at 524 °C. Besides, three new peaks centered at 670, 750 and 874 °C can be attributed to the overlapped reduction peaks of Ce and W ions in the bulk phase [44]. For the $Ce_1W_{0.24}Sn_2O_x$ catalyst, the broad peak in the range of 150−450 °C with maximum at 242 °C was assigned to the surface reduction of Sn^{4+}/Sn^{2+} and Ce^{4+}/Ce^{3+} [45]. The superimposed reduction peaks at 450−750 °C were mainly attributed to the reduction of Sn^{4+}/Sn^{2+}, Sn^{2+}/Sn^0 and Ce^{4+}/Ce^{3+} in the bulk phase [45]. With the increase in the hydrothermal aging temperature, the reduction peaks of the bulk phase shifted slightly towards higher temperature (Fig. 8b), which was related to the decreased mobility of lattice oxygen. However, the reduction peaks of surface species at 150−450 °C

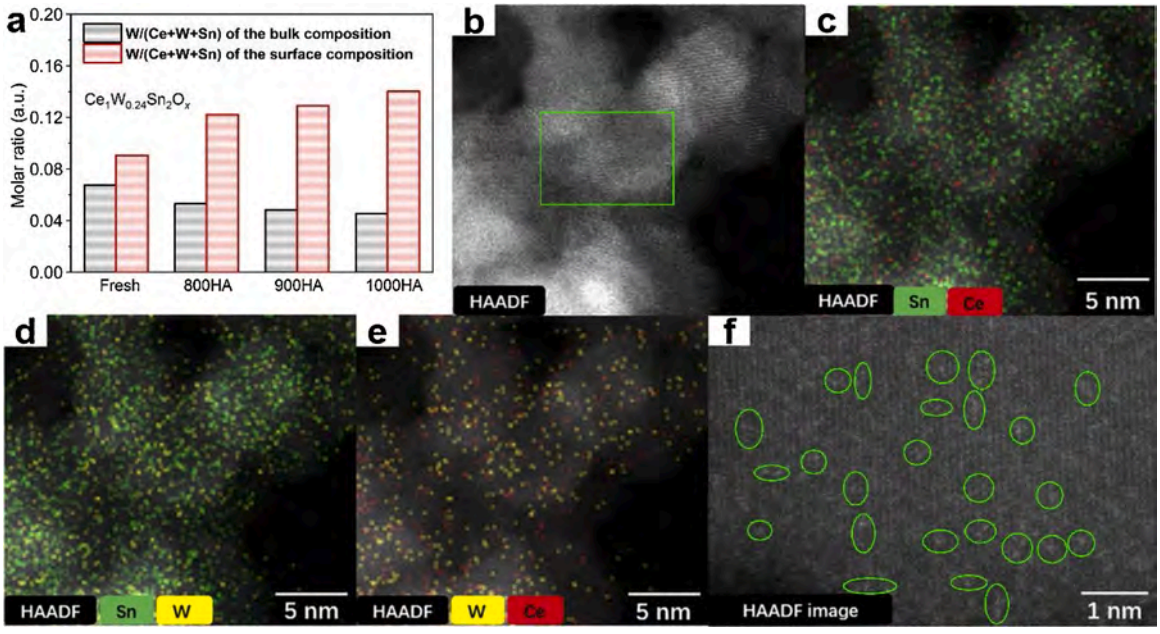

Fig. 6. Elemental composition and distribution. (a) The surface and bulk molar ratio of W/(Ce+W+Sn) for $Ce_1W_{0.24}Sn_2O_x$ catalysts calculated from XPS and XRF results, respectively. (b-e) HAADF-STEM images of SnO_2 particles in $Ce_1W_{0.24}Sn_2O_x$ catalyst. (f) HAADF image of SnO_2 particles in $Ce_1W_{0.24}Sn_2O_x$ catalyst at higher magnification.

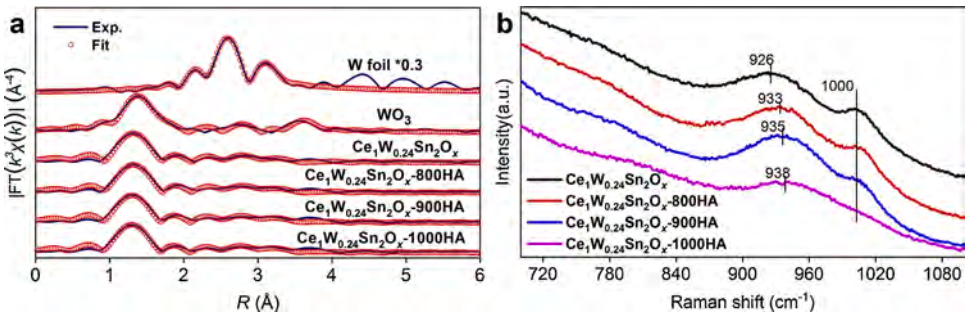

Fig. 7. Local structure of W species. (a) Comparison of W L_3-edge FT-EXAFS oscillations of W foil, WO_3 and $Ce_1W_{0.24}Sn_2O_x$ catalysts between the experimental and the fit curves. (b) *In situ* Raman spectra relating to W species of fresh and hydrothermally aged $Ce_1W_{0.24}Sn_2O_x$ catalysts at 300 °C.

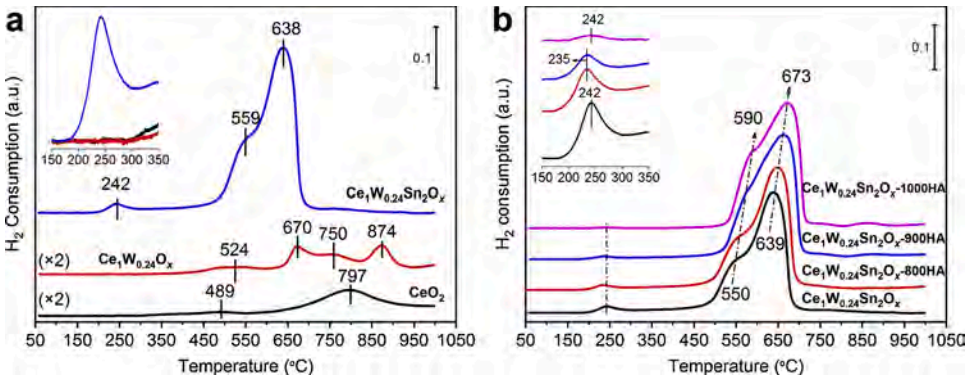

Fig. 8. Characterization of redox ability. (a) H_2-TPR profiles of fresh $Ce_1W_{0.24}Sn_2O_x$, $Ce_1W_{0.24}O_x$ and CeO_2 catalysts. (b) H_2-TPR profiles of hydrothermally aged $Ce_1W_{0.24}Sn_2O_x$ catalysts.

shifted towards lower temperature (Fig. 8b inset), indicating that the surface species of $Ce_1W_{0.24}Sn_2O_x$ were more reducible after the hydrothermal aging treatment. This can be related to the strong synergetic effects of surface Ce-W-Sn species due to the enrichment of Ce-W species on the surface of the SnO_2 phase. As verified by the NH_3-TPD results, the introduction of Sn into the $Ce_1W_{0.24}O_x$ catalyst modified the surface with abundant acid sites (Fig. 9a). Although a loss of acid sites took place after the hydrothermal aging treatment, the amounts of acid sites, when normalized to the surface area, did not show any significant change (Fig. 9b), indicating the outstanding stability of acid sites for $Ce_1W_{0.24}Sn_2O_x$ catalysts. Therefore, the addition of Sn benefits the preservation of redox and acid properties of the $Ce_1W_{0.24}Sn_2O_x$ catalyst, which is consistent with results for the V_2O_5/TiSnO_2 catalyst [31].

3.5. Theoretical calculations

According to the HR-TEM results (Fig. S9), the main exposed crystal plane of SnO_2 was (110) in the $Ce_1W_{0.24}Sn_2O_x$ catalyst. Thus, the formation energy of CeO_x, WO_x, and $CeWO_x$ species on the SnO_2 (110) surface ($E^f_{CeO_x/WO_x/CeWO_x}$)was calculated (Fig. 10a), which is defined as [46]

$$E^f_{CeO_x/WO_x/CeWO_x} = E_{CeO_x/WO_x/CeWO_x-loaded\ SnO_2} - E_{SnO_2} - E_{Ce/W} - \frac{x}{2}E_{O_2} \quad (4)$$

where $E_{CeO_x/WO_x/CeWO_x-loaded\ SnO_2}$, E_{SnO_2}, $E_{Ce/W}$ and E_{O_2} are the energies of CeO_x, WO_x, or $CeWO_x$ species supported on the substrate, the SnO_2 surface, the bulk Ce/W metal, and the gas-phase O_2, respectively. The negative formation energy represents the stabilization of CeO_x, WO_x, and $CeWO_x$ species on SnO_2 surfaces. The formation energy was -4.83,

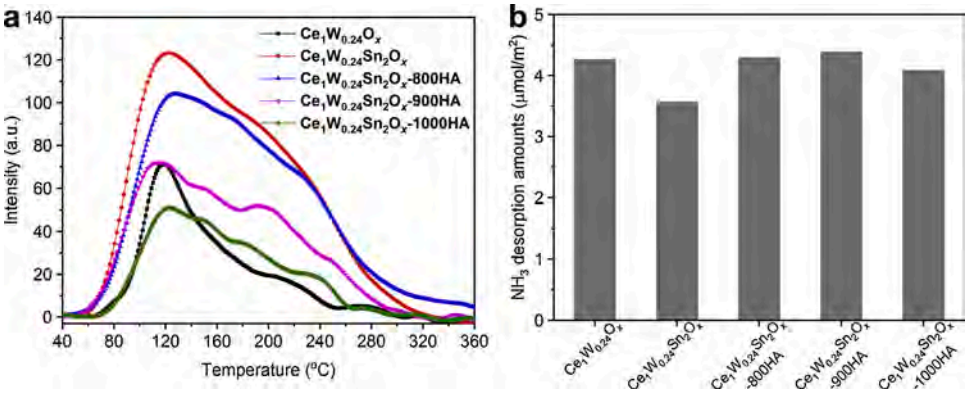

Fig. 9. Characterization of acidic property. (a) NH_3-TPD profiles of $Ce_1W_{0.24}O_x$ and $Ce_1W_{0.24}Sn_2O_x$ catalysts. (b) NH_3 desorption amounts of $Ce_1W_{0.24}O_x$ and $Ce_1W_{0.24}Sn_2O_x$ catalysts normalized by surface area.

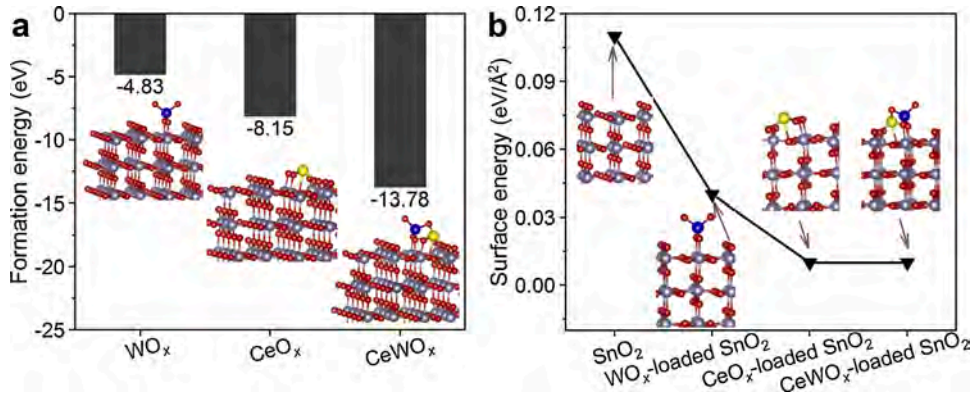

Fig. 10. DFT calculations. (a) The optimized geometries and the formation energies of WO_x, CeO_x and $CeWO_x$ species on SnO_2 (110) surfaces. (b) The optimized geometries and the surface energies of SnO_2 (110), and WO_x/ CeO_x/ $CeWO_x$ -loaded SnO_2 (110). The blue, red, purple, and yellow circles denote W, O, Sn, and Ce atoms, respectively. (For interpretation of the references to colour in this figure legend, the reader is referred to the web version of this article).

-8.15, and -13.78 eV for WO_x, CeO_x, and $CeWO_x$ on SnO_2, respectively, suggesting that $CeWO_x$ complex species are the most stable structure on the SnO_2 surface.

The surface energies of SnO_2 and CeO_x/WO_x/$CeWO_x$-loaded SnO_2 ($E^S_{SnO_2}$ and $E^S_{CeO_x/WO_x/CeWO_x-loaded\ SnO_2}$) were calculated to determine the effect of surface CeO_x, WO_x, and $CeWO_x$ species on structural stabilization (Fig. 10b). $E^S_{SnO_2}$ and $E^S_{CeO_x/WO_x/CeWO_x-loaded\ SnO_2}$ are respectively defined as [47]

$$E^S_{SnO_2} = \frac{1}{2A}\left[E^{Slab}_{SnO_2} - nE^{Bulk}_{SnO_2}\right] \tag{5}$$

$$E^S_{CeO_x/WO_x/CeWO_x-loaded\ SnO_2} = \frac{1}{2A}\left[E^{Slab}_{CeO_x/WO_x/CeWO_x-loaded\ SnO_2} - nE^{Bulk}_{SnO_2} - E_{Ce/W} - \frac{x}{2}E_{O_2}\right] \tag{6}$$

where A is the surface area of the slab, and $E^{Slab}_{SnO_2}$, $E^{Bulk}_{SnO_2}$, $E^{Slab}_{CeO_x/WO_x/CeWO_x-loaded\ SnO_2}$, $E_{Ce/W}$ and E_{O_2} are the energies of the SnO_2 surface, the bulk SnO_2, the CeO_x, WO_x, or $CeWO_x$ species supported on the SnO_2 surface, the bulk Ce/W metal, and the gas-phase O_2, respectively. The surface energy of the SnO_2 (110) crystal plane is predicted to be 0.11 eV $Å^{-2}$, which is respectively decreased to 0.04, 0.01, and 0.01 eV $Å^{-2}$ when there are WO_x, CeO_x, or $CeWO_x$ species on the surfaces, indicating that the loading of WO_x, CeO_x, and $CeWO_x$ species significantly enhances the structural stabilization.

4. Discussion

High temperature is detrimental to catalyst performance. After being heated at elevated temperatures, the amount of active sites on metal oxides can undergo significant loss mainly due to the migration and coalescence of particles (sintering) or through transport of monoatomic or molecular species between individual particles (Ostwald ripening) [48]. To develop stable catalysts, strategies such as increasing the metal-support interaction energy by using specific oxides as carriers, doping with suitable components, and encapsulation of individual colloidal nanoparticles in porous inorganic shells have attracted great attention [41,49,50]. However, the improvement of sintering resistance and the preservation of active catalytic sites has still remained a big challenge, especially for the fabrication of multicomponent catalysts.

CeO_2 undergoes relatively large changes in oxygen non-stoichiometry at temperatures below 1330 °C, which makes it possible to realize cycling between Ce^{3+}/Ce^{4+} to serve as redox sites for the NH_3-SCR reaction. However, pure CeO_2 is inactive (Fig. 1a), and only when closely coupled with other acidic elements (such as W in this work), can the CeO_2-based catalysts achieve superior $DeNO_x$ efficiency. According to previous reports [23,24], the appropriate coupling and high dispersion of Ce-W species contributed to the highly efficient $deNO_x$ capability of CeW-based catalysts. However, this situation mainly related to catalysts prepared at moderate temperatures such as 500 °C. Upon calcination or thermal shock at higher temperature, thermal sintering and solid-solid reaction would occur. In order to ensure the comparability of $Ce_1W_{0.24}O_x$ and $Ce_1W_{0.24}Sn_2O_x$ catalysts, the $Ce_1W_{0.24}O_x$ catalyst prepared in this work was calcined at 800 °C. According to the XRD results, besides the *c*-CeO_2 phase, the $Ce_4W_9O_{33}$ crystal phase was also detected for the fresh $Ce_1W_{0.24}O_x$ catalyst (Fig. 3a), suggesting that solid-solid reaction between CeO_2 and WO_x occurred during the calcination treatment. After being hydrothermally aged at 900 °C, solid phase reaction between $Ce_4W_9O_{33}$ and CeO_2 occurred, which accelerated the sintering of the $Ce_1W_{0.24}O_x$ catalyst and resulted in the release of more active oxygen species. Additionally, the phases *c*-CeO_2, $Ce_4W_9O_{33}$ and $Ce_2(WO_4)_3$ all sintered severely with the increase in temperature. As a result, lots of Ce-W dual sites were encapsulated within the stable bulk phase and lost their catalytic activity (Fig. 1c). With the introduction of SnO_2 into the $Ce_1W_{0.24}O_x$ catalyst, the crystallization and solid-solid reaction between Ce and W was significantly inhibited, and the obtained $Ce_1W_{0.24}Sn_2O_x$ catalyst showed excellent SCR performance even after extremely harsh aging treatment at 1000 °C (Fig. 1b). Such remarkable enhancement of thermal stability for this ternary $Ce_1W_{0.24}Sn_2O_x$ catalyst was due to the preservation of nanoscale SnO_2-related particles and their protective effects on the highly dispersed Ce-W active sites.

Although surface shrinkage also occurred for $Ce_1W_{0.24}Sn_2O_x$ catalyst after hydrothermal-aging (Fig. 2), the tungsten species not only maintained its highly dispersed state, but also coupled with Ce species to result in the formation of highly efficient Ce-O-W catalytic sites during aging treatment, thus contributing to the retention of NH_3-SCR activity even after being hydrothermally aged at 1000 °C. During the thermal decomposition process of the $Ce_1W_{0.24}Sn_2O_x$ precursor, part of the Ce atoms became incorporated into the SnO_2 lattice according to the Rietveld structure refinement (Table S1), which resulted in the formation of a Ce-doped SnO_2 solid solution. As a result, besides rapid formation of the *c*-CeO_2 phase, considerable amounts of Ce atoms were in close contact with the *t*-SnO_2 phase, and played a vital role in suppressing the sintering process of SnO_2 particles for the $Ce_1W_{0.24}Sn_2O_x$ catalyst. By further comparing the formation energies of CeO_x, WO_x and $CeWO_x$ on the SnO_2 (110) surface (Fig. 10a), it can be concluded that $CeWO_x$-loaded SnO_2 was the most stable configuration. In other words, CeO_x and WO_x species on the surface of SnO_2 tend to couple with each other to form $CeWO_x$ species, and thus serve as active sites for SCR reactions. After being hydrothermally aged at high temperature, Ce atoms in the *t*-SnO_2 unit cell tend to move towards the surface. Instead of

transferring to the surface of *c*-CeO_2 particles *via* Ostwald ripening, however, these Ce atoms tightly coupled with W species on the SnO_2 surface to form a stable $CeWO_x$-loaded SnO_2 structure, which was confirmed by HAADF and XAFS results (Figs. 6f and 7 a). Additionally, the high dispersion of $CeWO_x$ species on the surface of SnO_2 decreased the surface energy to a great extent (Fig. 10b), which in turn further inhibited the grain growth of SnO_2 particles and minimized thermal sintering reactions for the $Ce_1W_{0.24}Sn_2O_x$ catalyst. The improvement of sintering resistance and the preservation of highly dispersed Ce-W species induced by Sn is the main reason for the enhancement of hydrothermal stability for the $Ce_1W_{0.24}Sn_2O_x$ catalysts.

5. Conclusions

In summary, Sn was introduced to $Ce_1W_{0.24}O_x$ catalyst to develop a $Ce_1W_{0.24}Sn_2O_x$ ternary oxide catalyst with exceptional hydrothermal stability. Even after being hydrothermally aged at 1000 °C, the as-prepared $Ce_1W_{0.24}Sn_2O_x$ catalyst still removed >90 % NO_x from simulated diesel exhaust in the range 300−550 °C. The experimental and theoretical methods verified that SnO_2 promoted the formation of highly dispersed Ce-W active phase with superior thermal stability. Meanwhile, the Ce-W species localized on the SnO_2 particles remarkably decreased the surface energy and prevented the occurrence of sintering process at high temperature. As a result, the developed $Ce_1W_{0.24}Sn_2O_x$ catalyst is very promising for the application on diesel vehicles. Besides, other metal oxide catalysts that have an affinity to SnO_2 species could potentially be stabilized through the same strategy. Therefore, our study provides a new way towards developing catalysts with superior thermal stability.

CRediT authorship contribution statement

Jingjing Liu: Investigation, Formal analysis, Methodology, Writing - original draft. **Guangzhi He:** Methodology, Data curation, Writing - review & editing, Funding acquisition. **Wenpo Shan:** Formal analysis, Data curation, Supervision, Writing - review & editing, Funding acquisition, Project administration. **Yunbo Yu:** Data curation, Writing - review & editing, Funding acquisition. **Yanlong Huo:** Investigation, Formal analysis, Software. **Yan Zhang:** Investigation, Formal analysis. **Meng Wang:** Investigation, Formal analysis. **Rong Yu:** Investigation, Resources. **Shengsheng Liu:** Investigation, Resources. **Hong He:** Formal analysis, Data curation, Supervision, Writing - review & editing, Funding acquisition, Project administration.

Declaration of Competing Interest

The authors declare that they have no known competing financial interests or personal relationships that could have appeared to influence the work reported in this paper.

Acknowledgements

This work was supported by the Key Project of National Natural Science Foundation (21637005); the National Natural Science Foundation of China (51822811); the Youth Innovation Promotion Association of CAS (2019045); and K. C. Wong Education Foundation.

Appendix A. Supplementary data

Supplementary material related to this article can be found, in the online version, at doi:https://doi.org/10.1016/j.apcatb.2021.120125.

References

[1] P. Lanzafame, S. Perathoner, G. Centi, S. Gross, E.J.M. Hensen, Grand challenges for catalysis in the Science and Technology Roadmap on Catalysis for Europe: moving ahead for a sustainable future, Catal. Sci. Technol. 7 (2017) 5182–5194.
[2] M. Wang, B. Feng, H. Li, H. Li, Controlled assembly of hierarchical metal catalysts with enhanced performances, Chemistry 5 (2019) 805–837.
[3] E.D. Goodman, J.A. Schwalbe, M. Cargnello, Mechanistic understanding and the rational design of sinter-resistant heterogeneous catalysts, ACS Catal. 7 (2017) 7156–7173.
[4] L. Xu, H.W. Liang, Y. Yang, S.H. Yu, Stability and reactivity: positive and negative aspects for nanoparticle processing, Chem. Rev. 118 (2018) 3209–3250.
[5] A. Wang, L. Olsson, The impact of automotive catalysis on the United Nations sustainable development goals, Nat. Catal. 2 (2019) 566–570.
[6] R.J. Farrauto, M. Deeba, S. Alerasool, Gasoline automobile catalysis and its historical journey to cleaner air, Nat. Catal. 2 (2019) 603–613.
[7] C.H. Kim, G. Qi, K. Dahlberg, W. Li, Strontium-doped perovskites rival platinum catalysts for treating NO_x in simulated diesel exhaust, Science 327 (2010) 1624–1627.
[8] P.G. Smirniotis, D.A. Peña, B.S. Uphade, Low-temperature selective catalytic reduction (SCR) of NO with NH_3 by using Mn, Cr, and Cu oxides supported on Hombikat TiO_2, Angew. Chem. Int. Ed. 40 (2001) 2479–2482.
[9] M. Yu, D. Luss, V. Balakotaiah, Regeneration modes and peak temperatures in a diesel particulate filter, Chem. Eng. J. 232 (2013) 541–554.
[10] C. Paolucci, I. Khurana, A.A. Parekh, S. Li, A.J. Shih, A. Li, J.R. Di Iorio, J. D. Albarracin-Caballero, A. Yezerets, J.T. Miller, W.N. Delgass, F.H. Ribeiro, W. F. Schneider, R. Gounder, Dynamic multinuclear sites formed by mobilized copper ions in NO_x selective catalytic reduction, Science 357 (2017) 898–903.
[11] A. Marberger, A.W. Petrov, P. Steiger, M. Elsener, O. Kröcher, M. Nachtegaal, D. Ferri, Time-resolved copper speciation during selective catalytic reduction of NO on Cu-SSZ-13, Nat. Catal. 1 (2018) 221–227.
[12] Y.J. Kim, J.K. Lee, K.M. Min, S.B. Hong, I.-S. Nam, B.K. Cho, Hydrothermal stability of CuSSZ13 for reducing NO_x by NH_3, J. Catal. 311 (2014) 447–457.
[13] A.M. Beale, F. Gao, I. Lezcano-Gonzalez, C.H. Peden, J. Szanyi, Recent advances in automotive catalysis for NO_x emission control by small-pore microporous materials, Chem. Soc. Rev. 44 (2015) 7371–7405.
[14] T. Ryu, N.H. Ahn, S. Seo, J. Cho, H. Kim, D. Jo, G.T. Park, P.S. Kim, C.H. Kim, E. L. Bruce, P.A. Wright, I.S. Nam, S.B. Hong, Fully copper-exchanged high-silica LTA zeolites as unrivaled hydrothermally stable NH_3-SCR catalysts, Angew. Chem. Int. Ed. 56 (2017) 3256–3260.
[15] X. Ye, J.E. Schmidt, R.-P. Wang, I.K. van Ravenhorst, R. Oord, T. Chen, F. de Groot, F. Meirer, B.M. Weckhuysen, Deactivation of Cu-exchanged automotive-emission NH_3-SCR catalysts elucidated with nanoscale resolution using scanning transmission X-ray microscopy, Angew. Chem. Int. Ed. 59 (2020) 2–10.
[16] A. Marberger, D. Ferri, M. Elsener, O. Kröcher, The significance of Lewis acid sites for the selective catalytic reduction of nitric oxide on vanadium-based catalysts, Angew. Chem. Int. Ed. 55 (2016) 11989–11994.
[17] M. Zhu, J.K. Lai, U. Tumuluri, Z. Wu, I.E. Wachs, Nature of active sites and surface intermediates during SCR of NO with NH_3 by supported V_2O_5-WO_3/TiO_2 Catalysts, J. Am. Chem. Soc. 139 (2017) 15624–15627.
[18] G. Zhang, W. Han, H. Zhao, L. Zong, Z. Tang, Solvothermal synthesis of well-designed ceria-tin-titanium catalysts with enhanced catalytic performance for wide temperature NH_3-SCR reaction, Appl. Catal. B 226 (2018) 117–126.
[19] J. Liu, H. Cheng, J. Tan, B. Liu, Z. Zhang, H. Xu, M. Zhao, W. Zhu, J. Liu, Z. Zhao, Solvent-free rapid synthesis of porous $CeWO_x$ by a mechanochemical self-assembly strategy for the abatement of NO_x, J. Mater. Chem. A 8 (2020) 6717–6731.
[20] P. Granger, V.I. Parvulescu, Catalytic NO_x abatement systems for mobile sources: from three-way to lean burn after-treatment technologies, Chem. Rev. 111 (2011) 3155–3207.
[21] W. Qu, X. Liu, J. Chen, Y. Dong, X. Tang, Y. Chen, Single-atom catalysts reveal the dinuclear characteristic of active sites in NO selective reduction with NH_3, Nat. Commun. 11 (2020) 1532.
[22] W. Shan, Y. Yu, Y. Zhang, G. He, Y. Peng, J. Li, H. He, Theory and practice of metal oxide catalyst design for the selective catalytic reduction of NO with NH_3, Catal. Today (2020), https://doi.org/10.1016/j.cattod.2020.05.015.
[23] W. Shan, F. Liu, H. He, X. Shi, C. Zhang, Novel cerium-tungsten mixed oxide catalyst for the selective catalytic reduction of NO_x with NH_3, Chem. Commun. 47 (2011) 8046–8048.
[24] Y. Peng, K. Li, J. Li, Identification of the active sites on CeO_2-WO_3 catalysts for SCR of NO_x with NH_3: an *in situ* IR and Raman spectroscopy study, Appl. Catal. B 140 (2013) 483–492.
[25] M. Iwasaki, K. Dohmae, Y. Nagai, E. Sudo, T. Tanaka, Experimental assessment of the bifunctional NH_3-SCR pathway and the structural and acid-base properties of WO_3 dispersed on CeO_2 catalysts, J. Catal. 359 (2018) 55–67.
[26] A. Tricoli, M. Graf, S.E. Pratsinis, Optimal doping for enhanced SnO_2 sensitivity and thermal stability, Adv. Funct. Mater. 18 (2008) 1969–1976.
[27] M.W. Abee, D.F. Cox, NH_3 chemisorption on stoichiometric and oxygen-deficient SnO_2(1 1 0) surfaces, Surf. Sci. 520 (2002) 65–77.
[28] X. Tang, J. Li, L. Wei, J. Hao, MnO_x-SnO_2 catalysts synthesized by a redox coprecipitation method for selective catalytic reduction of NO by NH_3, Chin. J. Catal. 29 (2008) 531–536.
[29] X. Huang, G. Zhang, F. Dong, Z. Tang, The remarkable promotional effect of Sn on $CeVO_4$ catalyst for wide temperature NH_3-SCR process by citric acid-assisted solvothermal synthesis and post-hydrothermal treatment, Catal. Sci. Technol. 8 (2018) 5604–5615.

[30] Z. Hao, Y. Jiao, Q. Shi, H. Zhang, S. Zhan, Improvement of NH_3-SCR performance and SO_2 resistance over Sn modified $CeMoO_x$ electrospun fibers at low temperature, Catal. Today 327 (2019) 37–46.
[31] W. Si, H. Liu, T. Yan, H. Wang, C. Fan, S. Xiong, Z. Zhao, Y. Peng, J. Chen, J. Li, Sn-doped rutile $TiO_2$for vanadyl catalysts: Improvements on activity and stability in SCR reaction, Appl. Catal. B 269 (2020), 118797.
[32] L. Ren, L. Zhu, C. Yang, Y. Chen, Q. Sun, H. Zhang, C. Li, F. Nawaz, X. Meng, F. S. Xiao, Designed copper-amine complex as an efficient template for one-pot synthesis of Cu-SSZ-13 zeolite with excellent activity for selective catalytic reduction of NO_x by NH_3, Chem. Commun. 47 (2011) 9789–9791.
[33] J.P. Perdew, K. Burke, M. Ernzerhof, Generalized gradient approximation made simple, Phys. Rev. Lett. 77 (1996) 3865–3868.
[34] G. Kresse, J. Furthmuller, Efficient iterative schemes for *ab initio* total-energy calculations using a plane-wave basis set, Phys. Rev. B 54 (1996) 11169–11186.
[35] S. Suárez, S.M. Jung, P. Avila, P. Grange, J. Blanco, Influence of NH_3 and NO oxidation on the SCR reaction mechanism on copper/nickel and vanadium oxide catalysts supported on alumina and titania, Catal. Today 75 (2002) 331–338.
[36] L. Patout, D. Jacob, M. Arab, C. Pereira de Souza, C. Leroux, Monoclinic superstructure in orthorhombic $Ce_{10}W_{22}O_{81}$ from transmission electron microscopy, Acta Crystallogr. Sect. B: Struct. Sci. 70 (2014) 268–274.
[37] R.D. Shannon, Revised effective ionic radii and systematic studies of interatomic distances in halides and chalcogenides, Acta Crystallogr. Sect. A: Found. Crystallogr. 32 (1976) 751–767.
[38] A.P. Maciel, P.N. Lisbo-Filhoa, E.R. Leite, C.O. Paiva-Santos, W.H. Schreiner, Y. Maniette, E. Longo, Microstructural and morphological analysis of pure and Ce-doped tin dioxide nanoparticles, J. Solid State Chem. 23 (2003) 707–713.
[39] E.R. Leite, A.P. Maciel, I.T. Weber, P.N. Lisboa-Filho, E. Longo, C.O. Paiva-Santos, A.V.C. Andrade, C.A. Pakoscimas, Y. Maniette, W.H. Schreiner, Development of metal oxide nanoparticles with high stability against particle growth using a metastable solid solution, Adv. Mater. 14 (2002) 905–908.
[40] M. Yoshimura, F. Sibieude, A. Rouanet, M. Foex, Identification of binary compounds in the system Ce_2O_3-WO_3, J. Solid State Chem. 16 (1976) 219–232.
[41] S. Wang, A.Y. Borisevich, S.N. Rashkeev, M.V. Glazoff, K. Sohlberg, S. J. Pennycook, S.T. Pantelides, Dopants adsorbed as single atoms prevent degradation of catalysts, Nat. Mater. 3 (2004) 143–146.
[42] Y. Xin, N. Zhang, Q. Li, Z. Zhang, X. Cao, L. Zheng, Y. Zeng, J.A. Anderson, Active site identification and modification of electronic states by atomic-scale doping to enhance oxide catalyst innovation, ACS Catal. 8 (2018) 1399–1404.
[43] G. Sui, Z. Xue, D. Zhou, Y. Wang, Y. Shen, Y. Zong, Y. Liu, T. Qiu, S. Zhu, The influence factors on $CeSn_{0.8}W_{0.6}O_x/TiO_2$ for catalytic removals of NO, CO and C_3H_8, J. Ind. Eng. Chem. 51 (2017) 229–236.
[44] T. Zhang, F. Qiu, H. Chang, Y. Peng, J. Li, Novel W-modified $SnMnCeO_x$ catalyst for the selective catalytic reduction of NO_x with NH_3, Catal. Commun. 100 (2017) 117–120.
[45] R. Sasikala, N.M. Gupta, S.K. Kulshreshtha, Temperature-programmed reduction and CO oxidation studies over Ce-Sn mixed oxides, Catal. Lett. 71 (2001) 69–73.
[46] I. Song, J. Lee, G. Lee, J.W. Han, D.H. Kim, Chemisorption of NH_3 on monomeric vanadium oxide supported on anatase TiO_2: a combined DRIFT and DFT study, J. Phys. Chem. C 122 (2018) 16674–16682.
[47] R. Tran, Z. Xu, B. Radhakrishnan, D. Winston, W. Sun, K.A. Persson, S.P. Ong, Surface energies of elemental crystals, Sci. Data 3 (2016), 160080.
[48] G. Prieto, J. Zecevic, H. Friedrich, K.P. de Jong, P.E. de Jongh, Towards stable catalysts by controlling collective properties of supported metal nanoparticles, Nat. Mater. 12 (2013) 34–39.
[49] J.A. Farmer, C.T. Campbell, Ceria maintains smaller metal catalyst particles by strong metal-support bonding, Science 329 (2010) 933–936.
[50] S.H. Joo, J.Y. Park, C.K. Tsung, Y. Yamada, P. Yang, G.A. Somorjai, Thermally stable Pt/mesoporous silica core-shell nanocatalysts for high-temperature reactions, Nat. Mater. 8 (2009) 126–131.